RESEARCH ARTICLE

Femtosecond laser-acoustic modeling and simulation for AlCu nanofilm nondestructive testing

Zhongyu WANG[a], **Jing MIN**[a], **Jing HU**[a], **Zehan WANG**[a], **Xiuguo CHEN**[a,b], **Zirong TANG** (✉)[a,b], **Shiyuan LIU** (✉)[a,b]

[a] State Key Laboratory of Intelligent Manufacturing Equipment and Technology, Huazhong University of Science and Technology, Wuhan 430074, China
[b] Optics Valley Laboratory, Wuhan 430074, China

✉ Corresponding authors. Emails: zirong@hust.edu.cn (Zirong TANG); shyliu@hust.edu.cn (Shiyuan LIU)

ABSTRACT Photoacoustic detection has shown excellent performance in measuring thickness and detecting defects in metal nanofilms. However, existing research on ultrafast lasers mainly focuses on using picosecond or nanosecond lasers for large-scale material processing and measurement. The theoretical study of femtosecond laser sources for photoacoustic nondestructive testing (NDT) in nanoscale thin film materials receives much less emphasis, leading to a lack of a complete physical model that covers the entire process from excitation to measurement. In this study, we developed a comprehensive physical model that combines the two-temperature model with the acoustic wave generation and detection model. On the basis of the physical model, we established a simulation model to visualize the ultrafast laser-material interaction process. The damage threshold of the laser source is determined, and the effect of key parameters (laser fluence, pulse duration, and wavelength) for AlCu nanofilms on the femtosecond photoacoustic NDT process is discussed using numerical results from the finite element model. The numerical results under certain parameters show good agreement with the experimental results.

1 Introduction

Photoacoustic detection, a technique using acoustic waves generated by pulsed laser absorption in materials, has gained recognition for its capability in noninvasively probing the structural and material properties of thin films [1–6]. Particularly in the field of metal nanofilms, this method has demonstrated remarkable success in measuring film thickness and identifying defects with nanoscale accuracy [7,8]. Metal nanofilms, given their pivotal roles in various applications, such as electronics, optics, and material science [9–11], necessitate advanced techniques for accurate characterization to ensure that their performance meets the stringent requirements of these applications.

The advent of ultrafast lasers, characterized by their extremely short pulse durations, has revolutionized

material processing and measurement. In ultrafast laser-matter interactions, the laser pulse excites electrons without heating the lattice, leading to nonequilibrium heating. This distinct thermal response, because of the short duration of the laser pulse compared with the major characteristic times between electrons and lattice, requires treating their temperatures as separate subsystems [12]. As a result, the traditional thermoelasticity theory, which assumes equilibrium conditions, is inadequate for ultrafast laser-matter interactions [13]. To tackle this issue, models such as the two-temperature model (TTM), hot-electron blast model, and ultrafast thermoelasticity model have been developed and have a great implementation in high-intensity ultrashort laser processing [14–16]. Benefiting from their capacity to achieve substantial material modifications with minimal thermal side effects, ultrafast laser sources have become a popular choice for processing and structuring metal materials [17–19].

The utilization of ultrafast laser sources for thin film measurement enables the attainment of increased acoustic

frequencies, reaching up to hundreds of GHz. This capability makes them ideal for analyzing materials with high temporal and spatial resolution. Studies on acoustic wave generation across various metal films, such as Au [20], Ag [21], Al [22,23], Cr [24], Pt [25], Ni [1], and W [26,27], have been conducted to leverage this capability. Despite these efforts, a comprehensive physical model that spans the entire process from laser excitation to photoacoustic signal measurement is still missing. This absence forces researchers to depend on trial and error, tweaking laser parameters through experimental means to enhance signal quality and ascertain the damage threshold for nondestructive testing (NDT) across different materials or laser specifications. This approach is necessitated because the photoacoustic detection process is significantly influenced by the laser parameters and the physical properties of the metal films, which together determine the intensity of photoacoustic signals [27].

Our study addresses this need by introducing a comprehensive physical model that combines the TTM with an acoustic wave generation and detection model. The TTM, which separates electron and lattice temperatures, lays a solid foundation for comprehending the rapid dynamics induced by femtosecond laser irradiation. Integrating such dynamics with a model for acoustic wave generation and detection gives us a full picture of the photoacoustic testing. We develop a simulation model that visually depicts the entire physical processes of femtosecond photoacoustic testing in metal nanofilms. The damage thresholds of laser sources for AlCu nanofilms are determined, and the effects of key laser parameters, including laser fluence, pulse duration, and wavelength, on the photoacoustic signal are explored. Through detailed analysis and comparison with experimental data for specific parameters, our study demonstrates that the proposed model can accurately predict the outcome of femtosecond photoacoustic NDT in metal nanofilms. This study provides valuable insights for improving photoacoustic detection in metal nanofilm characterization and paves the way for enhanced characterization techniques for metal nanofilms.

2 Theoretical framework

2.1 Temperature distribution of electrons and lattice

In our study, the pump beam's illuminated area (20 μm × 15 μm) is much larger than the laser absorption depth and the film's thickness, which usually varies from tens to hundreds of nanometers. Accordingly, a simple one-directional model was chosen for our analysis. The temporal and spatial evolutions of the electron and lattice temperatures are calculated in accordance with TTM [13], shown as follows:

$$C_e(T_e)\frac{\partial T_e}{\partial t} = \frac{\partial}{\partial z}\left(\kappa_e\frac{\partial T_e}{\partial z}\right) - G(T_e - T_l) + Q, \qquad (1)$$

$$C_l(T_l)\frac{\partial T_l}{\partial t} = G(T_e - T_l), \qquad (2)$$

where C is the specific heat, T is the temperature field, κ is the thermal conductivity, G is the electron–lattice coupling factor, and Q is the volumetric laser heat source. The subscripts e and l represent the electrons and lattice, respectively.

Equations (1) and (2) are based on the premise that heat transport in the electron and lattice system follows the classical Fourier law. This assumption is valid for laser pulses longer than several tens of femtoseconds [28]. The diffusion term in Eq. (2) is ignored because the timescale of heat accumulation is significantly longer than that of a single pulse irradiation.

Under the present experimental setup, we selected a Gaussian laser beam in both time and space as the laser source. The volumetric heat source generated by the laser energy deposition can be expressed as follows [29,30]:

$$Q(z,t) = \sqrt{\frac{\beta}{\pi}}\frac{(1-\delta)J_0}{t_p z_s(1-e^{-L/z_s})}\exp\left[-\frac{z}{z_s}-\beta\left(\frac{t-2t_p}{t_p}\right)^2\right], \quad (3)$$

where δ is the surface reflectivity, J_0 is the peak fluence (at $z = 0$) carried by laser pulse, and t_p is the laser pulse duration, which is defined as the full width at half maximum intensity of a laser pulse; z_s is the optical penetration depth; L is the film thickness. $\beta = 4\ln2$.

2.2 Generation of strain pluses

In solid photoacoustic, the essence of acoustic pulses stems from the thermoelastic stress induced by ultrashort laser pulses. Once the temperature distribution is calculated, we can establish the physical model for the generation and propagation of acoustic waves. In this one-directional model, we assume that the metal film is elastically isotropic. This assumption allows us to express the thermal stress as follows:

$$\sigma_{T_{ij}} = -(2\mu + 3\lambda)\alpha\delta_{ij}\Delta T(z,t), \qquad (4)$$

where μ is the shear modulus, λ is the Lamé constant, α is the thermal expansion coefficient, δ_{ij} is the Kronecker delta function, and ΔT is the change in temperature compared with a reference temperature T_0. Because the only motion of the lattice is parallel to the z-axis and the only nonzero strain under this uniaxial condition is ε_{zz}, the three normal stress components can be expressed as follows:

$$\sigma_{zz} = (2\mu + \lambda)\varepsilon_{zz} - (2\mu + 3\lambda)\alpha\Delta T(z,t), \qquad (5)$$

$$\sigma_{xx} = \sigma_{yy} = \lambda\varepsilon_{zz} - (2\mu + 3\lambda)\alpha\Delta T(z,t). \qquad (6)$$

In solid materials, the Lamé constant λ, the shear

modulus μ, and the bulk modulus B can be expressed as follows:

$$\lambda = E \frac{\upsilon}{(1+\upsilon)(1-2\upsilon)}, \tag{7}$$

$$\mu = \frac{E}{2(1+2\upsilon)}, \tag{8}$$

$$B = \frac{E}{3(1-2\upsilon)}, \tag{9}$$

where E is the Young's modulus, υ is the Poisson's ratio, and B is the bulk modulus. Therefore, Eqs. (5) and (6) can be rewritten as follows:

$$\sigma_{zz} = (2\mu+\lambda)\varepsilon_{zz} - 3B\alpha\Delta T(z,t) = 3\frac{1-\upsilon}{1+\upsilon}B\varepsilon_{zz} - 3B\alpha\Delta T(z,t), \tag{10}$$

$$\sigma_{xx} = \sigma_{yy} = \lambda\varepsilon_{zz} - 3B\alpha\Delta T(z,t). \tag{11}$$

In this one-directional model, in which motion is solely parallel to the z-axis and no shear stresses exist, we can express the effective stress σ_{eff} for the von Mises criterion as follows:

$$\sigma_{\text{eff}} = \frac{1}{\sqrt{2}}\left[(\sigma_{xx}-\sigma_{yy})^2 + (\sigma_{yy}-\sigma_{zz})^2 + (\sigma_{zz}-\sigma_{xx})^2\right]^{1/2}$$
$$= 2\mu|\varepsilon_{zz}|. \tag{12}$$

The applied stress state will lead to yielding when the magnitude of σ_{eff} reaches a critical threshold. Thus, the effective stress is a key indicator of material failure.

The equation for deformation and wave propagation along the z-axis, often analyzed as a wave equation with zero body forces, can be expressed as follows:

$$\rho\frac{\partial^2 u_z}{\partial t^2} = \frac{\partial \sigma_{zz}}{\partial z}, \tag{13}$$

where ρ is the density, and u_z is the displacement in the z-axis direction. Substituting σ_{zz} from Eq. (10) into Eq. (13), the momentum equation in terms of the displacement and the temperature distribution can be expressed as follows:

$$\rho\frac{\partial^2 u_z}{\partial t^2} = 3\frac{1-\upsilon}{1+\upsilon}B\frac{\partial^2 u_z}{\partial z^2} - 3B\alpha\frac{\partial T}{\partial z}. \tag{14}$$

From Eq. (14), the underlying physical processes behind the generation and propagation of acoustic pulses, induced by femtosecond laser pulses in metal nanofilms, are elucidated.

2.3 Detection of strain pluses

To detect high-frequency acoustic signals reaching up to hundreds of GHz, we employ the time-delayed pump-probe technique, as illustrated in Fig. 1. This method measures changes in the surface reflectivity of the metal nanofilm. These changes happen because the propagating strain pulses modify the optical properties of the material
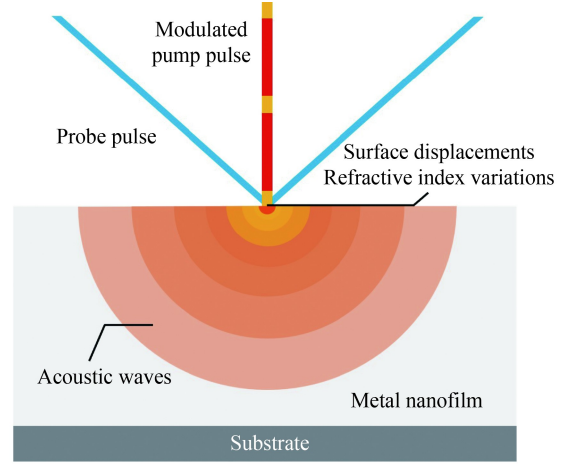

Fig. 1 Schematic of the pump-probe technique.

upon reaching the subsurface of metal nanofilms. In our setup, the pump pulse and the probe pulse are derived from the same laser source, which means that they have identical wavelengths. The angle of incidence for the probe pulse is typically set between 5° and 45°.

The variation in the complex index of refraction (Δn and $\Delta\kappa$) of the metal nanofilm surface can be described as follows:

$$\Delta n(z,t) = \frac{\partial n}{\partial \varepsilon_{zz}}\varepsilon_{zz}(z,t), \tag{15}$$

$$\Delta\kappa(z,t) = \frac{\partial \kappa}{\partial \varepsilon_{zz}}\varepsilon_{zz}(z,t). \tag{16}$$

On this basis, we can establish a relationship between the change in the dielectric constant ($\Delta\varepsilon$) of the solid medium and the alterations in the refractive index induced by the propagating strain, as shown as follows:

$$\Delta\varepsilon(z,t) = \varepsilon - \varepsilon' \cong 2(n+i\kappa)\left(\frac{dn}{d\eta} + i\frac{d\kappa}{d\eta}\right)\varepsilon_{zz}(z,t), \tag{17}$$

where $dn/d\eta$ and $d\kappa/d\eta$ are photoelastic constants that depend on laser wavelength [31]. To calculate the change in reflectivity due to variations in the dielectric constant within the solid medium, the Maxwell's equations inside the metal film can be expressed by

$$\frac{\partial^2 E}{\partial z^2} = -k^2[\varepsilon + \Delta\varepsilon(z,t)]E, \tag{18}$$

where k is the free-space wave number. Through solving Maxwell's equations, the total reflected electric field, when strain perturbation $\Delta\varepsilon = F\delta(z-z')$ exists only at a distance z', can be computed as follows:

$$rE^{(0)} = \left(r_0 + \frac{iFkt_0\tilde{t}_0}{2\tilde{n}}e^{2ik\tilde{n}z'}\right)E^{(0)}, \tag{19}$$

where r_0, t_0, and $\tilde{t}_0$ are reflection and transmission coefficients, which can be calculated using Fresnel equations; $\tilde{n}$ is the complex refractive index ($\tilde{n} = n + i\kappa$).

If we now consider the more general case of an arbitrary $\Delta\varepsilon(z',t)$, then the reflection coefficient can be expressed as follows:

$$r = r_0 + \frac{\mathrm{i}k}{2\tilde{n}} t_0 \tilde{t}_0 \int_0^\infty \Delta\varepsilon(z',t)\, \mathrm{e}^{2\mathrm{i}k\tilde{n}z'}\, \mathrm{d}z'. \qquad (20)$$

Through combining these results and simplifying, the change in reflectivity δR can be expressed as follows:

$$\delta R(t) = \int_0^\infty f(z)\varepsilon_{zz}(z,t)\, \mathrm{d}z, \qquad (21)$$

$$f(z) = f_0\left[\frac{\partial n}{\partial\eta}\sin\left(\frac{4\pi nz}{\lambda}-\phi\right)+\frac{\partial\kappa}{\partial\eta}\cos\left(\frac{4\pi nz}{\lambda}-\phi\right)\right]\mathrm{e}^{-z/z_s}, \qquad (22)$$

where

$$f_0 = 8\frac{\omega[n^2(n^2+\kappa^2-1)+\kappa^2(n^2+\kappa^2+1)]^{1/2}}{c\left[(n+1)^2+\kappa^2\right]}, \qquad (23)$$

$$\phi = \arctan\left[\frac{\kappa(n^2+\kappa^2+1)}{n(n^2+\kappa^2-1)}\right]. \qquad (24)$$

3   Numerical simulation

To visualize the ultrafast laser-material interaction in femtosecond photoacoustic NDT of metal nanofilms, we establish a one-dimensional simulation model based on the physical model. The main framework of this simulation model is depicted in Fig. 2. In our study, we use the finite difference method to solve the heat conduction equation and determine the temperature field distribution in metal nanofilms. Meanwhile, the finite element method helps us solve the momentum equation to find the stress and strain distribution in the nanofilms. For simplicity, we use identical grid meshes for both numerical methods.

For our simulation model, we selected a 500 nm-thick AlCu nanofilm composed of 95% aluminum and 5% copper. The mesh is evenly divided along the depth (z-axis), with each cell having a length of 2 nm, resulting in a total of 250 elements. A laser source with a pulse duration of 107 fs (1 fs = 10^{-15} s), an energy per pulse of 4 nJ (equivalent to a peak laser fluence of 35 J/m²), and a wavelength of 920 nm is used. Given the reasonably low laser fluence (T_e < 3200 K), the electron–lattice coupling factor G can be assumed to be a constant [32]. The specific heat of the electron can be expressed as $C_e = C_0 \cdot T_e$ and the electron thermal conductivity as $\kappa_e = \kappa_1 \cdot T_e/T_1$. The right boundary of the model (top of the nanofilm) is set to convective heat transfer with air, the left boundary (bottom of the nanofilm) to contact heat transfer with a silicon substrate, and the initial temperature T_0 to 300 K. The thermophysical and optical properties of the materials are listed in Table 1. The distribution of the laser heat source, as determined by the simulation model, is depicted in Figs. 3(a) and 3(b), and the resulting temperature distribution for the electronic and lattice systems during the ultrafast laser-material interaction is illustrated in Figs. 3(c) and 3(d).

Figures 3(a) and 3(b) illustrate the simulation results of the energy conversion from optical to thermal during the femtosecond laser-matter interaction in AlCu nanofilms. In Fig. 3(a), the blue curve shows the laser fluence profile on the nanofilm surface, while the other curves depict the volumetric laser heat source profiles on the material surface and at depths of 5, 20, and 50 nm. The energy absorption by the metal nanofilm from the laser
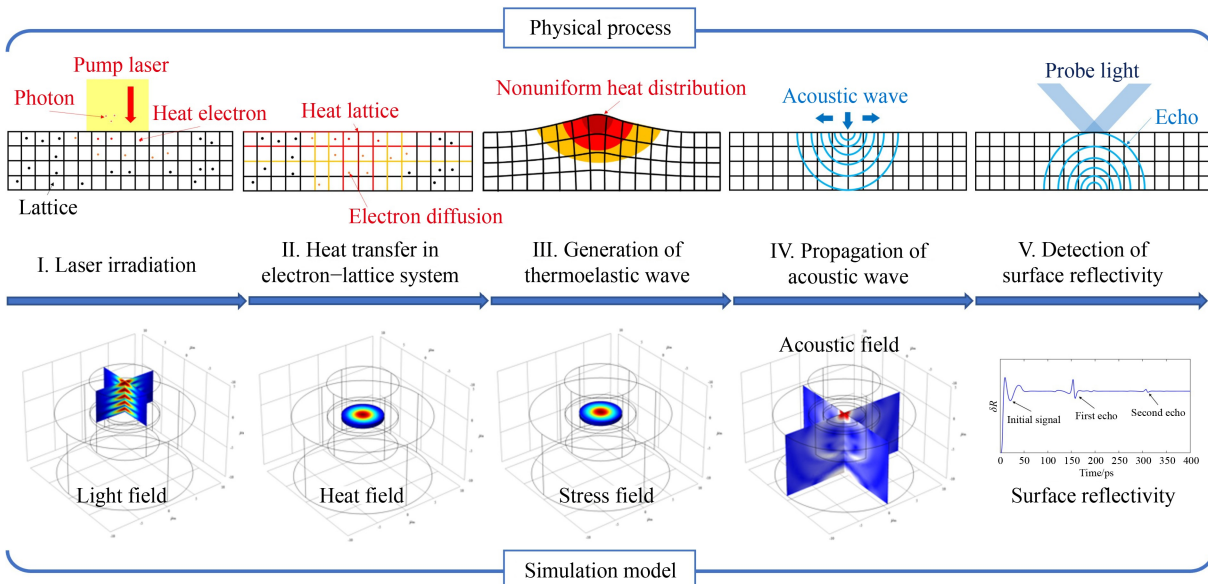

Fig. 2   Main framework of the simulation model.

Table 1 Thermophysical and optical properties of AlCu nanofilms

Description	Symbol	Value	Unit
Reference specific heat of the electron	C_0	135	J/m³·K
Thermal conductivity of the lattice	κ_l	237	W/m·K
Surface reflectivity for a wavelength of 920 nm	δ	0.907	–
Optical penetration depth for a wavelength of 920 nm	z_s	9.640	nm
Poisson's ratio	υ	0.350	–
Specific heat of the lattice	C_l	2.42×10^6	J/m³·K
Electron–lattice coupling factor	G	3.10×10^{17}	–
Young's modulus	E	70×10^9	Pa
Shear modulus	μ	26×10^9	Pa
Thermal expansion coefficient	α	23.1×10^{-6}	1/K
Density	ρ	2.70×10^3	kg/m³
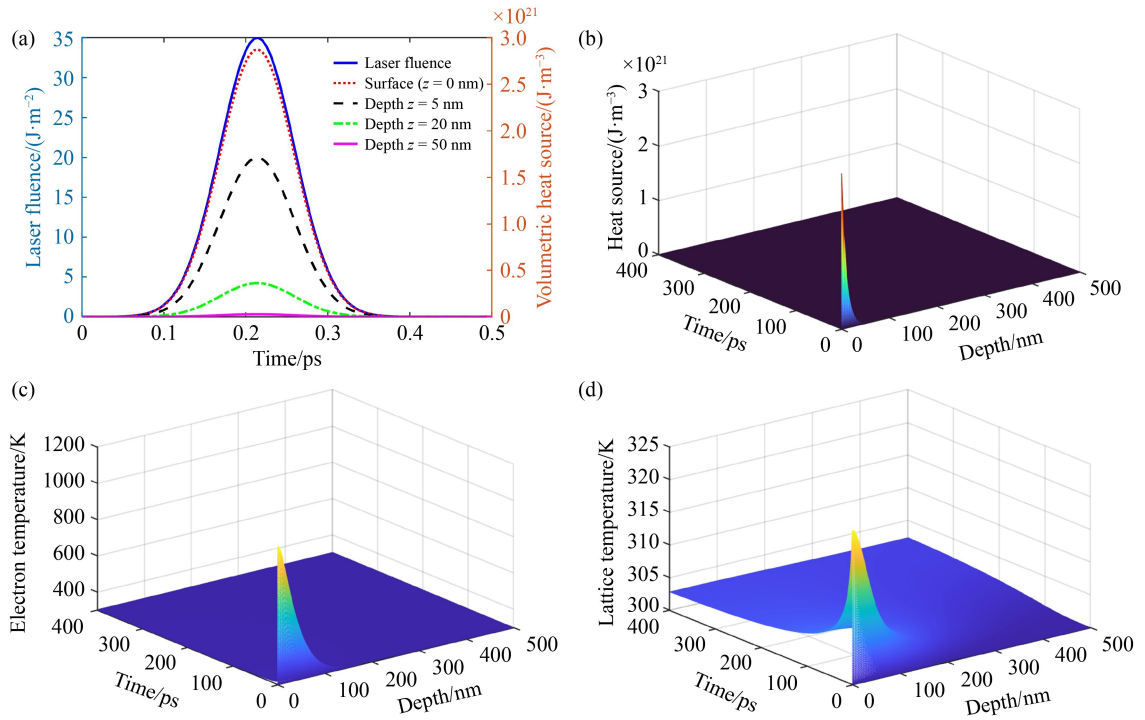
Fig. 3 (a) Profile of the laser heat source in various depths. (b) Temporal and spatial distribution of the laser heat source. (c) Temporal and spatial distribution of the electron temperature. (d) Temporal and spatial distribution of the lattice temperature.

irradiation is highest on the material surface and decreases with depth. Beyond 50 nm, the absorbed energy is significantly lower than that on the surface. Notably, the trend of the volumetric laser heat source profile at different depths aligns with the laser fluence profile, both exhibiting a Gaussian distribution. They both sharply rise from the start, peak at approximately 0.215 ps (1 ps = 10^{-12} s), and then quickly fall, nearing zero around 0.43 ps. Figure 3(b) displays the volumetric laser heat source as a function of time and depth, highlighting that the heat source's time distribution is concentrated in a brief interval near the start, due to the ultrashort pulse duration of the laser. Spatially, the volumetric laser heat

source peaks near the surface and decreases sharply with depth, mirroring the conductive heat behavior in metal nanofilms.

Figures 3(c) and 3(d) present the thermal dynamics of heat transfer from the volumetric laser heat source to the electronic and lattice systems during femtosecond laser-matter interaction in AlCu nanofilms. Figure 3(c) shows how the electron temperature varies with time and depth, peaking at 1056.9 K on the material surface around 0.255 ps before quickly dropping. The electron temperature sharply falls off with depth, indicating that the high-temperature region is concentrated near the material subsurface. For comparison, Fig. 3(d) displays the

changes in lattice temperature over time and depth, which are more evenly distributed than the electron temperature. The lattice temperature's peak is much lower, reaching a maximum of 323.36 K on the surface around 0.805 ps. The simulation results accurately depict the temperature distribution of the electronic and lattice systems in metal nanofilms, consistent with the two-temperature process in the physical model. The electronic system initially absorbs the heat and subsequently transfers the energy to the lattice system, where energy transfer and diffusion occur much more slowly.

After solving the temporal and spatial temperature distribution in the AlCu nanofilm, we can simulate the acoustic signal, including the stress and strain distribution in the material. For the numerical solution, we use the finite element method with the same grid mesh as in the previous step. At each time step, the strain field is calculated by differentiating the displacement field. Thermal stress is determined on the basis of the strain and temperature fields, described by Eq. (10), which serve as the source term for the wave equation. The strain and temperature fields are updated with every new time step.

The right boundary of the finite element model is set as a free boundary. The left boundary, which is the bottom of the film in contact with the base material, is defined as an absorption boundary. When acoustic pulses hit the interface between different materials, only part of the pulse reflects back, while the rest transmits into the adjacent medium. The reflectivity of the sound pulse is calculated by $R_S = (Z_i - Z_e)/(Z_i + Z_e)$, where Z_i and Z_e represent the acoustic impedance of incident and emergent media, respectively. With this formula, the boundary condition at the bottom of the model is established as follows:

$$u_z(z_L, t) = u_z(z_L, t-1) + (1 - R_S)v_l$$
$$\cdot \frac{\mathrm{d}t}{\mathrm{d}z}[u_z(z_{L-1}, t-1) - u_z(z_L, t-1)], \quad (25)$$

where t and z are the time step and element length, respectively. v_l is the longitude velocity of the acoustic wave in the material. z_L represents the bottom node of the

model. The calculated stress distribution in the nanofilm at various times is presented in Fig. 4 (a), and the temporal and spatial evolution of the internal strain field is depicted in Fig. 4 (b).

Figures 4(a) and 4(b) display the simulation outcomes of energy conversion from thermal to acoustic during femtosecond photoacoustic interactions in AlCu nanofilms. The uneven thermal field distribution causes thermal stress and strain, which then propagate as acoustic signals. Figure 4(a) shows the longitude stress profiles within the nanofilm at various times. The black line indicates the acoustic pressure distribution at 0.6 ps, while other colored curves show distributions at 25, 50, and 75 ps. Generally, as time progresses, the fluctuations and amplitude of acoustic pressure decrease and spread in the depth direction. Figure 4(b) presents a color contour map showing the spatial and temporal distribution of strain in the nanofilm. Initially, strain emerges on the surface of nanofilms and moves deeper. Upon reaching the interface, reflection and phase inversion create a distinct wave pattern, illustrating the dynamic stress waves in nanofilms due to ultrafast laser irradiation.

The final step involves integrating the subsurface strain field of the AlCu nanofilm to capture the temporal evolution of changes in surface reflectivity of the material. This evolution corresponds to the photoacoustic signal measured in our experiments. Figure 5 displays the change in surface reflectivity of the AlCu nanofilm as calculated by our numerical simulation model.

As shown in Fig. 5, the reflectivity change signal clearly presents an initial signal near the initial time due to laser irradiation, and the first and second echoes are observed at approximately 155 and 310 ps, respectively. These echoes result from the acoustic signal being reflected at the interface and propagating back to the subsurface of the nanofilm, causing changes in its optical properties. The fluctuation and amplitude of δR gradually decrease with each reflection. The timing of these echoes aligns with the strain distribution numerical results depicted in Fig. 4(b). Figure 5 also presents the final output of the femtosecond photoacoustic simulation model we developed.
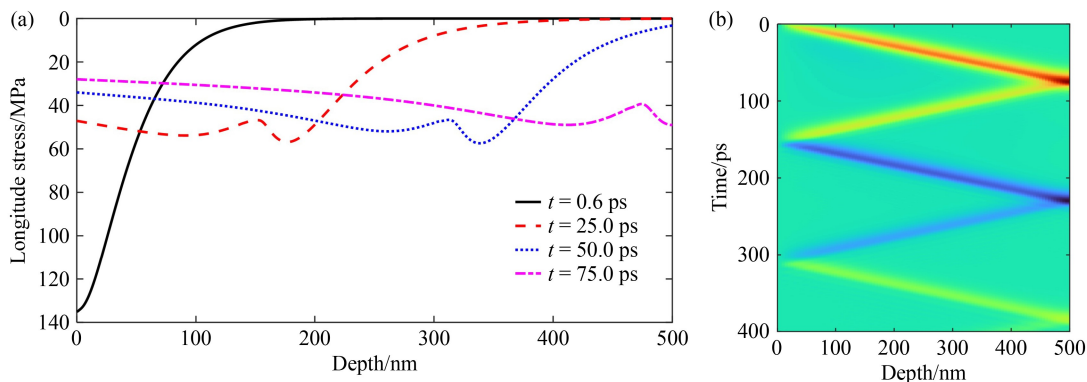

Fig. 4   (a) Profile of longitude stress in the nanofilm at various times. (b) Temporal and spatial distribution of the strain in the nanofilm.

4   Results and discussion

4.1   Damage threshold of AlCu nanofilms

To prevent surface damage or phase transformation in metal nanofilms, the laser fluence used in nanofilm photoacoustic NDT is typically kept below tens of mJ/cm^2. At this low level of laser energy density, damage from the hot-electron blast force, which occurs when the electron temperature reaches the order of the Fermi temperature (usually around 10^4 K for metals), can be disregarded [33]. Consequently, potential damage mechanisms are categorized into thermal (melting) and nonthermal (high-stress damage) [34]. To identify the laser fluence threshold for photoacoustic NDT without causing material damage, we calculated the maximum effective stress and the temperatures of electrons and lattice in the 500 nm AlCu nanofilm under laser fluences ranging from 0.2 to 20 mJ/cm^2, as depicted in Figs. 6 (a) and 6(b). The laser operates at a wavelength of 920 nm and a pulse duration of 107 fs.

From Fig. 6(a), the effective stress induced by the laser pulse in the metal film reaches the yield strength of the material (500 MPa for the 500 nm AlCu nanofilm) at a laser fluence of 17.2 mJ/cm^2. The areas representing high-stress damage and the nondestructive zone are marked in red and blue, respectively. Figure 6(b) shows that the
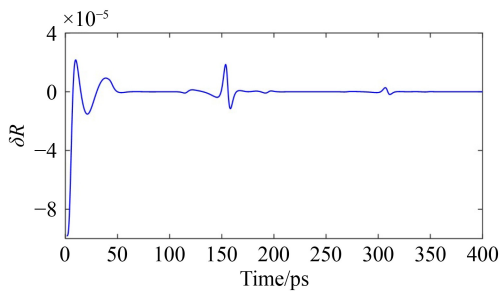
maximum electron and lattice temperatures rise with increasing laser fluence, with $T_{e,max}$ and $T_{l,max}$ peaking at a laser fluence of 20 mJ/cm^2. The highest recorded $T_{e,max}$ and $T_{l,max}$ under the strongest pump laser fluence (20 mJ/cm^2) are 2594.69 and 405.55 K, respectively. These temperatures are significantly lower than the Fermi temperature (1.36×10^5 K for AlCu) and melting point (635 K for AlCu). Accordingly, the laser fluence threshold for conducting NDT in 500 nm AlCu nanofilms, under 920 nm wavelength and 107 fs pulse duration, is 17.2 mJ/cm^2. The material will likely experience high-stress damage before thermal damage.

The yield strength of metal nanofilms is highly dependent on the length scale and typically exhibits its maximum value at thicknesses ranging from tens to a few hundred nanometers, depending on the grain size [35]. In such cases, the damage mechanism and threshold can also be analyzed and calculated using this model.

4.2   Influence of key laser parameters

As mentioned earlier, the key parameters of the laser source significantly affect the intensity of the photoacoustic signal. To enhance the signal quality, it's crucial to understand how these parameters affect the physical processes and signal intensity and identify the optimal combination of laser parameters within the damage threshold of nanofilms. In this section, we explore the influence of key laser parameters on signal intensity using our model. We first calculate and discuss the numerical results for a 500 nm AlCu film irradiated by various laser fluences, as presented in Fig. 7. We selected a laser wavelength of 920 nm and a pulse duration of 107 fs, with the laser fluence ranging from 0.2 to 15 mJ/cm^2 to stay below the NDT threshold of nanofilms.

Figures 7(a) and 7(b) display the calculated heating times and maximum temperatures of electrons and the lattice in a 500 nm-thick AlCu film under varying laser pulse fluence. The heating time is the duration required to reach their maximum temperatures ($T_{e,max}$ and $T_{l,max}$). In Fig. 7(a), the electron heating time slightly increases from

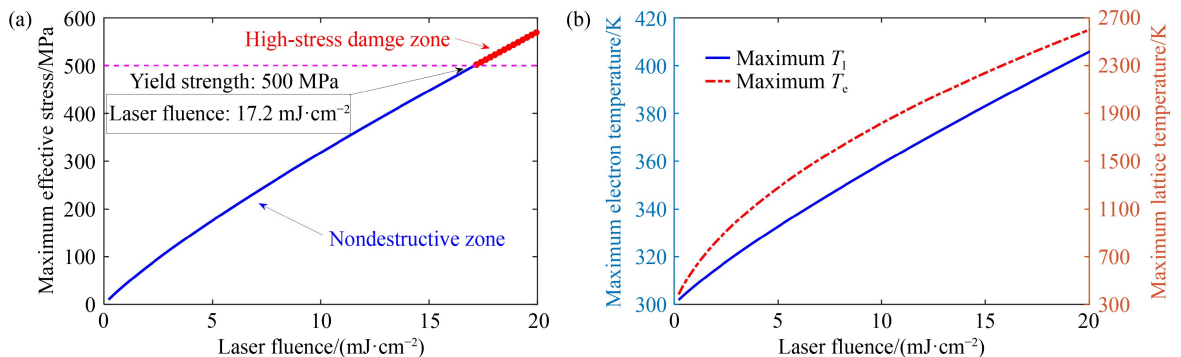**Fig. 5**   Temporal evolution of the change in surface reflectivity.

Fig. 6   (a) Maximum effective stress in nanofilms under varying laser fluence. (b) Maximum electron and lattice temperatures in nanofilms under varying laser fluence.

0.25 to 0.26 ps as the laser fluence rises from 0.2 to 4.7 mJ/cm² and stabilizes at 0.26 ps for fluences between 4.7 and 15 mJ/cm². Meanwhile, the lattice heating time extends from 0.63 to 1.10 ps across the entire range of laser fluence. Figure 7(b) illustrates the values of $T_{\mathrm{e,max}}$ and $T_{\mathrm{l,max}}$ under different laser fluences. A pronounced increase in $T_{\mathrm{e,max}}$ (from 383.28 to 2227.94 K) occurs with the fluence rising from 0.2 to 15 mJ/cm², while $T_{\mathrm{l,max}}$ experiences a more gradual increase (from 301.84 to 382.37 K) throughout the laser fluence range. Figures 7(a) and 7(b) clearly depict the nonequilibrium process induced in the metal film by the ultrashort laser.

Figure 7(c) presents the calculated maximum effective stress generated during the photoacoustic process. Similar to $T_{\mathrm{l,max}}$, $\sigma_{\mathrm{eff,max}}$ linearly increases from 9.90 to 443.97 MPa as the laser fluence grows from 0.2 to 15 mJ/cm². This increase is attributed to the temperature gradient within the metal lattice, which causes thermoelastic stress. The amplitude of the first photoacoustic echo, represented as the signal intensity of δR, under varying laser fluence, is depicted in Fig. 7(d). δR escalates with increasing laser fluence.

$T_{\mathrm{e,max}}$, $T_{\mathrm{l,max}}$, $\sigma_{\mathrm{eff,max}}$, and δR all increase with rising laser fluence. These findings underscore that laser fluence is a key factor affecting the intensity and quality of photoacoustic signals. Thus, increasing laser fluence under the same parameters is a straightforward and effective method to boost the photoacoustic signal intensity. For photoacoustic detection, selecting a laser source with the maximum feasible fluence within the damage threshold can significantly enhance signal intensity.

In photoacoustic detection, changing the laser wavelength affects the surface reflectivity and optical penetration depth of the metal film, thereby influencing the laser energy absorption and volumetric laser heat distribution. Through the complex refractive index of the nanofilm, measured experimentally, the influence of laser wavelength λ on surface reflectivity δ can be calculated with the Fresnel formula [36]. The connection between laser wavelength λ and optical penetration depth z_s is given by $z_s = \lambda/(4\pi k)$, where k represents the complex index of refraction of the metal film. These relationships and their effects are depicted in Figs. 8(a) and 8(b).

The numerical results for a 500 nm-thick AlCu film irradiated with varying laser wavelengths are presented in Fig. 9. We selected a laser fluence of 3.4 mJ/cm² and a pulse duration of 107 fs. The range of laser wavelengths tested spans from 400 to 1200 nm.

Figure 9(a) demonstrates how the laser wavelength influences the heating times of electrons and lattice. The electron heating time peaks briefly at 0.26 ps for wavelengths between 820 and 870 nm, remaining at 0.255 ps across other wavelengths. By contrast, the lattice heating time extends from 0.77 to 0.88 ps as the wavelength increases from 400 to 830 nm, then decreases to 0.71 ps for wavelengths from 830 to 1200 nm. Comparison of Figs. 8 and 9 reveals a similarity in the
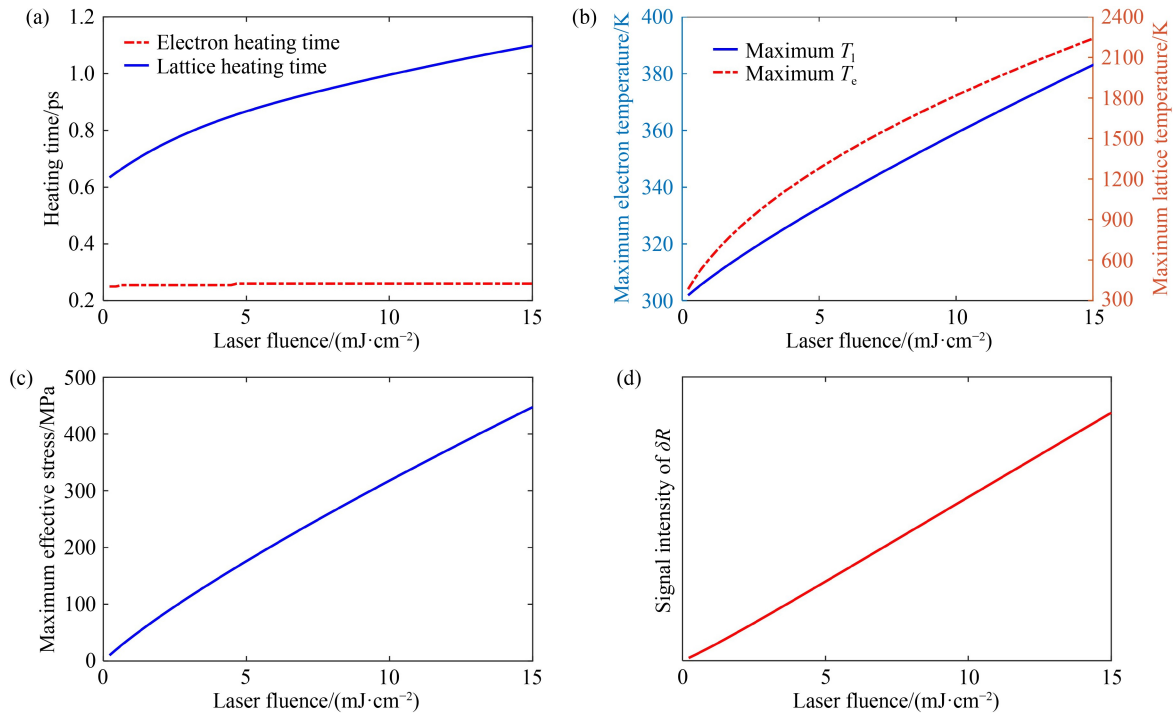

Fig. 7   (a) Electron and lattice heating time in nanofilms under varying laser fluence. (b) Maximum electron and lattice temperatures in nanofilms under varying laser fluence. (c) Maximum effective stress in nanofilms under varying laser fluence. (d) Signal intensity of δR under varying laser fluence.
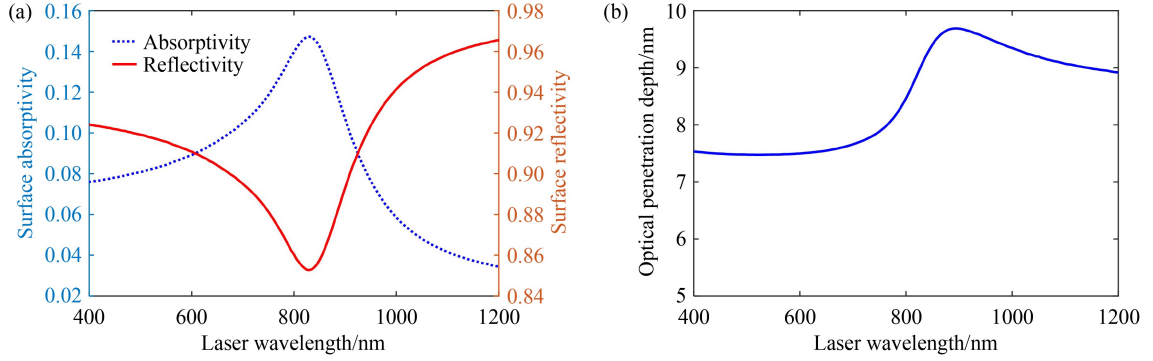
Fig. 8 (a) Surface reflectivity and absorptivity of AlCu nanofilms under varying laser wavelength. (b) Optical penetration depth of AlCu nanofilms under varying laser wavelength.
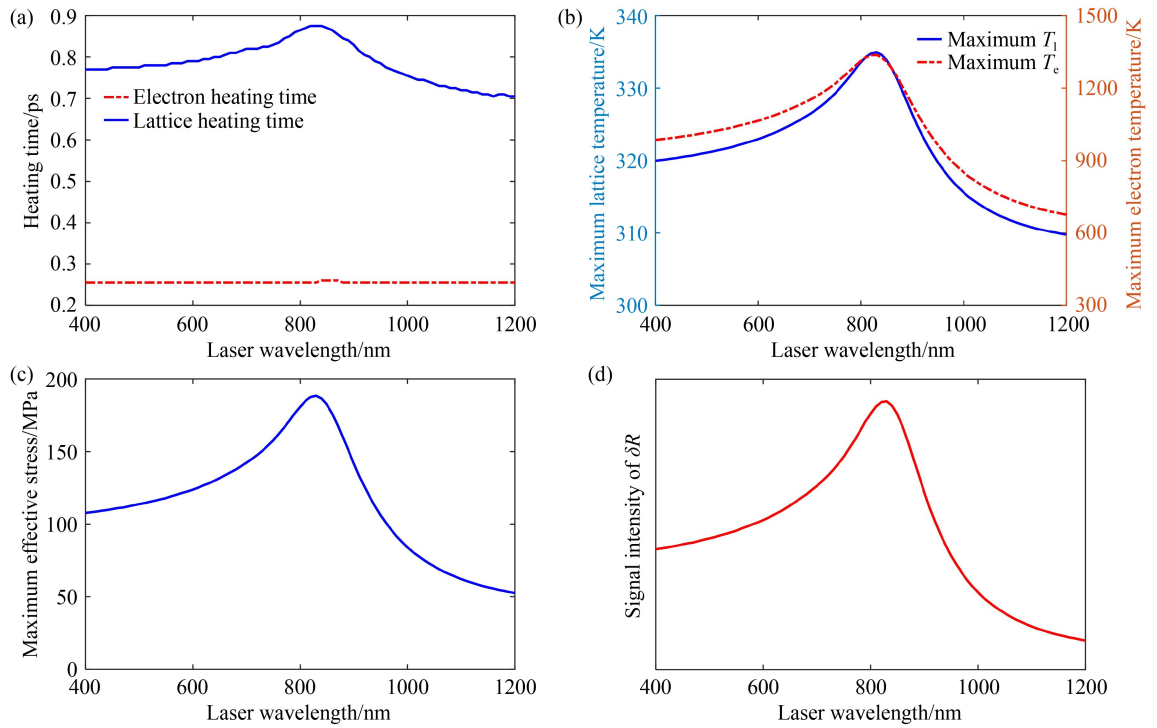

Fig. 9 (a) Electron and lattice heating time in nanofilms under varying laser wavelength. (b) Maximum electron and lattice temperatures in nanofilms under varying laser wavelength. (c) Maximum effective stress in nanofilms under varying laser wavelength. (d) Signal intensity of δR under varying laser wavelength.

trend of heating times, particularly for the lattice, with wavelength changes mirroring the surface absorptivity of the nanofilm. This similarity exists because the energy absorption in ultrafast laser-matter interactions is governed by surface absorptivity $1 - \delta$ and optical penetration depth z_s, with the absorption rate change playing a crucial role. The surface absorptivity of AlCu films reaches its peak at 830 nm wavelength. Consequently, the substantial energy absorbed by the nanofilm lengthens the time needed for the lattice and electronic systems to reach their peak temperatures. However, the electron heating time is less influenced by laser wavelength changes than the lattice heating time.

Similarly, Figs. 9(b)–9(d) show a comparable pattern:

$T_{e,max}$, $T_{l,max}$, $\sigma_{eff,max}$, and δR all initially increase with the laser wavelength, peak at 830 nm, and then gradually decline as the wavelength continues to rise. This pattern indicates that the effect of laser wavelength on the photoacoustic process in metal nanofilms operates through a similar mechanism as laser fluence. Both parameters alter the energy absorbed by the metal film, thereby changing the temperature and stress–strain distribution and ultimately affecting the photoacoustic signal intensity. The numerical results suggest that the AlCu nanofilm optimally absorbs laser pulses at a wavelength of 830 nm. Therefore, laser sources near this wavelength should be preferred to enhance signal intensity in photoacoustic NDT.

To explore the effect of pulse duration on photoacoustic detection, we calculated the numerical results for a 500 nm AlCu film irradiated by pump pulses of varying durations, as depicted in Fig. 10. The laser wavelength and fluence were set to 920 nm and 3.4 mJ/cm^2, respectively. The range of pulse durations span from 50 to 800 fs, ensuring that they remain shorter than the major relaxation times of the metal film and that the heating process follows a two-step mechanism.

In Fig. 10(a), the electron and lattice heating times increase with the pump pulse duration. This result shows that longer pulse durations extend the energy conversion from optical to thermal in ultrafast laser-matter interactions. Furthermore, Fig. 10(b) indicates that the maximum electron temperature $T_{e,max}$ decreases from 1248.59 to 557.66 K as the pulse duration lengthens, while the maximum lattice temperature $T_{l,max}$ slightly rises from 322.76 to 325.58 K. This trend suggests that longer pulse durations, despite the total energy of each pulse being fixed, allow more energy to transfer to the lattice system owing to the extended electron heating time. Consequently, the nonequilibrium characteristics between the electron and lattice systems are diminished, leading to a decrease in $T_{e,max}$ and a slight increase in $T_{l,max}$.

In Figs. 10(c) and 10(d), the maximum effective stress $\sigma_{eff,max}$ and signal intensity of δR increase as the pulse duration extends from 50 to 800 fs. As previously discussed, we hypothesize that longer pulse durations enhance laser-matter interactions, facilitating greater energy transfer to the lattice, which is then converted into acoustic waves. These findings indicate that pulse duration has a lesser effect on the photoacoustic signal intensity compared with laser fluence and wavelength. Therefore, enhancing the photoacoustic signal intensity could involve increasing the laser pulse duration. However, the pulse duration must remain shorter than all the electron–lattice relaxation times.

4.3 Comparison with experimental results

To verify the accuracy and correctness of our model, we performed an experiment using a 500 nm-thick AlCu nanofilm. The laser source chosen for this experiment had a pulse duration of 107 fs, a power of 320 mW, a wavelength of 920 nm, a repetition frequency of 80 MHz, and a spot size of 20 μm × 15 μm (with a corresponding laser fluence of 3.4 mJ/cm^2). We compared the numerical results obtained from the simulation model, under identical parameters, with the experimental outcomes. This comparison is presented in Fig. 11.

As illustrated in Fig. 11, the simulated results of our model align closely with the experimental data, especially in the echo region. The model accurately predicts the amplitude, phase, and timing of the echo signal. However, the model significantly underestimates the amplitude of the initial signal peak. This discrepancy
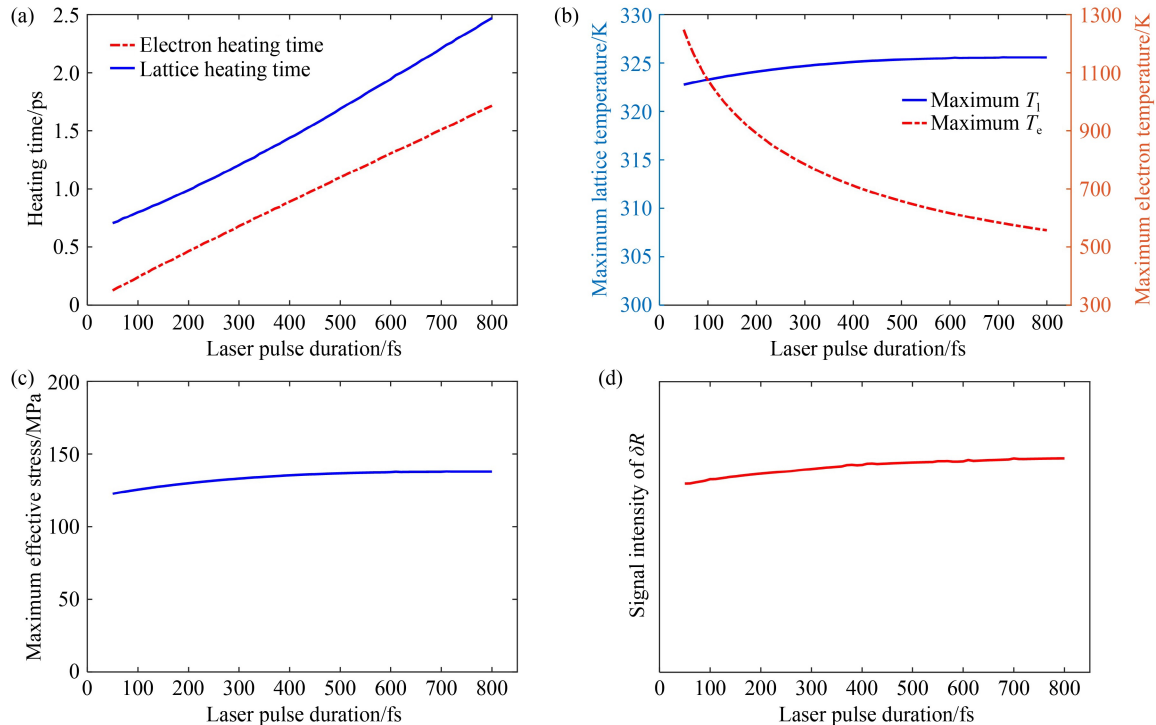

Fig. 10 (a) Electron and lattice heating time in nanofilms under varying pulse duration. (b) Maximum electron and lattice temperatures in nanofilms under varying pulse duration. (c) Maximum effective stress in nanofilms under varying pulse duration. (d) Signal intensity of δR under varying laser pulse duration.
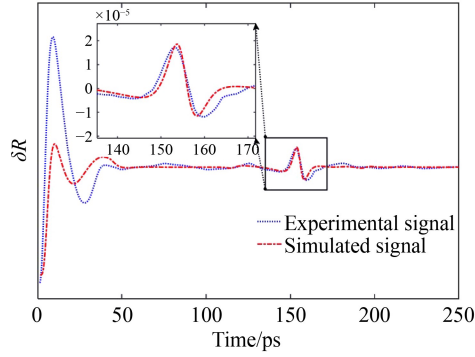
Fig. 11   Comparison diagram of experimental and simulated signals.

likely stems from the rapid changes in electron and lattice temperatures at the initial moment of ultrafast laser-matter interaction, which alter the optical properties of the metal nanofilm. This observation suggests the need for further model refinement in subsequent studies.

5   Conclusions

In this study, we have developed a comprehensive physical model for pump-probe femtosecond photoacoustic NDT in metal nanofilms. This model includes laser-matter interaction, heat distribution and conduction within electron and lattice systems, generation and propagation of acoustic pulses, and changes in surface reflectivity caused by strain pulses. Moreover, a simulation model aligned with the physical model has been established. This simulation allows us to calculate and visualize key parameters and physical characteristics, such as temperature distributions of electrons and lattice, strain pulse distribution, and acoustic wave magnitude. These elements are difficult to measure experimentally, making our model crucial for a thorough understanding of the femtosecond photoacoustic NDT process in metal nanofilms. Additionally, we investigated the damage threshold for 500 nm AlCu metal nanofilms and analyzed how key laser parameters (fluence, wavelength, and pulse duration) affect the ultrafast laser-matter interaction and photoacoustic signal intensity. On the basis our findings, we offer recommendations for optimizing laser source parameters. The comparison between simulated signal and experimental data shows strong agreement in the echo signal region.

Nomenclature

Abbreviations

NDT	Nondestructive testing
TTM	Two-temperature model

Variables

B	Bulk modulus
C_0	Reference specific heat of the electron
C_e	Electron specific heat
C_l	Lattice specific heat
E	Young's modulus
G	Electron–lattice coupling factor
J_0	Peak fluence carried by laser pulse
k	Free-space wave number
L	Film thickness
$\tilde{n}$	Complex refractive index
Q	Volumetric laser heat source
R_S	Reflectivity of the sound pulse
r_0	Reflection coefficient
T_e	Electron temperature
T_l	Lattice temperature
t_0	Transmission coefficient
t_p	Laser pulse duration
v_l	Longitude velocity of acoustic wave
z_e	Acoustic impedance of emergent medium
z_i	Acoustic impedance of incident medium
z_s	Optical penetration depth
α	Thermal expansion coefficient
ε	Strain
κ_e	Electron thermal conductivity
κ_l	Lattice thermal conductivity
δ	Surface reflectivity
δR	Change in reflectivity
λ	Lamé constant
δ_{ij}	Kronecker delta function
ρ	Density
σ_{eff}	Effective stress
μ	Shear modulus
υ	Poisson's ratio

References

1. Thomsen C, Grahn H T, Maris H J, Tauc J. Surface generation and detection of phonons by picosecond light pulses. Physical Review B, 1986, 34(6): 4129–4138

2. Dubois M, Drake Jr. T E. Evolution of industrial laser-ultrasonic systems for the inspection of composites. Nondestructive Testing and Evaluation, 2011, 26(3–4): 213–228

3. Matsuda O, Larciprete M C, Li Voti R, Wright O B. Fundamentals of picosecond laser ultrasonics. Ultrasonics, 2015, 56: 3–20

4. Manohar S, Razansky D. Photoacoustics: a historical review. Advances in Optics and Photonics, 2016, 8(4): 586–617

5. Hurley D H. Pump-probe laser ultrasonics: characterization of material microstructure. IEEE Nanotechnology Magazine, 2019, 13(3): 29–38

6. Zhang K X, Chen D, Wang S, Yao Z J, Feng W, Guo S F. Flexible and high-intensity photoacoustic transducer with PDMS/CSNPs nanocomposite for inspecting thick structure using laser ultrasonics. Composites Science and Technology, 2022, 228: 109667

7. Antonelli G A, Maris H J, Malhotra S G, Harper J M E. Picosecond ultrasonics study of the vibrational modes of a nanostructure. Journal of Applied Physics, 2002, 91(5): 3261–3267

8. Chou K Y, Wu C L, Shen C C, Sheu J K, Sun C K. Terahertz photoacoustic generation using ultrathin nickel nanofilms. Journal of Physical Chemistry C, 2021, 125(5): 3134–3142

9. Ji G N, Zhu W Y, Jia X X, Ji S F, Han D P, Gao Z X, Liu H, Wang Y, Han T. AuNP/Cu-TCPP(Fe) metal-organic framework nanofilm: a paper-based electrochemical sensor for non-invasive detection of lactate in sweat. Nanoscale, 2023, 15(10): 5023–5035

10. Zheng S, Wang C G, Li J X, Wang W Q, Yu Q, Wang C W, Wang S Q. Graphene oxide-based three-dimensional au nanofilm with high-density and controllable hotspots: a powerful film-type SERS tag for immunochromatographic analysis of multiple mycotoxins in complex samples. Chemical Engineering Journal, 2022, 448: 137760

11. Rodriguez-Davila R A, Chapman R A, Shamsi Z H, Castillo S J, Young C D, Quevedo-López M A. Low temperature, highly stable ZnO thin-film transistors. Microelectronic Engineering, 2023, 279: 112063

12. Gamaly E G. The physics of ultra-short laser interaction with solids at non-relativistic intensities. Physics Reports, 2011, 508(4–5): 91–243

13. Anisimov S I, Kapeliovich B L, Perel'man T L. Electron emission from metal surfaces exposed to ultrashort laser pulses. Journal of Experimental and Theoretical Physics, 1974, 39(2): 375–377

14. Falkovsky L A, Mishchenko E G. Electron-lattice kinetics of metals heated by ultrashort laser pulses. Journal of Experimental and Theoretical Physics, 1999, 88(1): 84–88

15. Chen J K, Beraun J E, Grimes L E, Tzou D Y. Modeling of femtosecond laser-induced non-equilibrium deformation in metal films. International Journal of Solids and Structures, 2002, 39(12): 3199–3216

16. Povarnitsyn M E, Andreev N E, Apfelbaum E M, Itina T E, Khishchenko K V, Kostenko O F, Levashov P R, Veysman M E. A wide-range model for simulation of pump-probe experiments with metals. Applied Surface Science, 2012, 258(23): 9480–9483

17. Ancona A, Döring S, Jauregui C, Röser F, Limpert J, Nolte S, Tünnermann A. Femtosecond and picosecond laser drilling of metals at high repetition rates and average powers. Optics Letters, 2009, 34(21): 3304–3306

18. Heise G, Trappendreher D, Ilchmann F, Weiss R S, Wolf B, Huber H. Picosecond laser structuring of thin film platinum layers covered with tantalum pentoxide isolation. Journal of Applied Physics, 2012, 112(1): 013110

19. Bonse J, Krüger J. Structuring of thin films by ultrashort laser pulses. Applied Physics A, 2023, 129(1): 14

20. Del Fatti N, Voisin C, Christofilos D, Vallée F, Flytzanis C. Acoustic vibration of metal films and nanoparticles. The Journal of Physical Chemistry A, 2000, 104(18): 4321–4326

21. Yamaguchi S, Tahara T. Coherent acoustic phonons in a thin gold film probed by femtosecond surface plasmon resonance. Journal of Raman Spectroscopy, 2008, 39(11): 1703–1706

22. Grossmann M, Schubert M, He C, Brick D, Scheer E, Hettich M, Gusev V, Dekorsy T. Characterization of thin-film adhesion and phonon lifetimes in Al/Si membranes by picosecond ultrasonics. New Journal of Physics, 2017, 19(5): 053019

23. Grossmann M, Klingele M, Scheel P, Ristow O, Hettich M, He C, Waitz R, Schubert M F, Bruchhausen A E, Gusev V E, Scheer E, Dekorsy T. Femtosecond spectroscopy of acoustic frequency combs in the 100-GHz frequency range in Al/Si membranes. Physical Review B, 2013, 88(20): 205202

24. Saito T, Matsuda O, Wright O B. Picosecond acoustic phonon pulse generation in nickel and chromium. Physical Review B, 2003, 67(20): 205421

25. O'hara K E, Hu X Y, Cahill D G. Characterization of nanostructured metal films by picosecond acoustics and interferometry. Journal of Applied Physics, 2001, 90(9): 4852–4858

26. Richardson C J K, Ehrlich M J, Wagner J W. Interferometric detection of ultrafast thermoelastic transients in thin films: theory with supporting experiment. Journal of the Optical Society of America B: Optical Physics, 1999, 16(6): 1007–1015

27. Devos A, Lerouge C. Evidence of laser-wavelength effect in picosecond ultrasonics: possible connection with interband transitions. Physical Review Letters, 2001, 86(12): 2669–2672

28. Anisimov S I, Rethfeld B. Theory of ultrashort laser pulse interaction with a metal. In: KonovV I, Libenson M N, eds. Nonresonant Laser-Matter Interaction (NLMI-9). St. Petersburg: SPIE, 1997, 192–203

29. Qiu T Q, Tien C L. Femtosecond laser heating of multi-layer metals—I. Analysis. International Journal of Heat and Mass Transfer, 1994, 37(17): 2789–2797

30. Qiu T Q, Juhasz T, Suarez C, Bron W E, Tien C L. Femtosecond laser heating of multi-layer metals—II. Experiments. International Journal of Heat and Mass Transfer, 1994, 37(17): 2799–2808

31. Matsuda O, Wright O B. Reflection and transmission of light in multilayers perturbed by picosecond strain pulse propagation. Journal of the Optical Society of America B: Optical Physics, 2002, 19(12): 3028–3041

32. Lin Z B, Zhigilei L V, Celli V. Electron-phonon coupling and

electron heat capacity of metals under conditions of strong electron-phonon nonequilibrium. Physical Review B, 2008, 77(7): 075133

33. Chen J K, Beraun J E, Tzou D Y. Thermomechanical response of metal films heated by ultrashort-pulsed lasers. Journal of Thermal Stresses, 2002, 25(6): 539–558

34. Kittle C. Introduction to Solid State Physics. New York: John Wiles & Sons, 1967

35. Zhang J Y, Zhang X, Liu G, Wang R H, Zhang G J, Sun J. Length scale dependent yield strength and fatigue behavior of nanocrystalline Cu thin films. Materials Science and Engineering: A, 2011, 528(25–26): 7774–7780

36. McPeak K M, Jayanti S V, Kress S J P, Meyer S, Iotti S, Rossinelli A, Norris D J. Plasmonic films can easily be better: rules and recipes. ACS Photonics, 2015, 2(3): 326–333